Intravoxel Incoherent Motion Modeling in the Kidneys: Comparison of Mono-, Bi-, and Triexponential Fit

Sophie van Baalen, Msc,[1]* Alexander Leemans, PhD,[2] Pieter Dik, MD, PhD,[3] Marc R. Lilien, MD, PhD,[4] Bennie ten Haken, PhD,[1] and Martijn Froeling, PhD[5]

Purpose: To evaluate if a three-component model correctly describes the diffusion signal in the kidney and whether it can provide complementary anatomical or physiological information about the underlying tissue.
Materials and Methods: Ten healthy volunteers were examined at 3T, with T_2-weighted imaging, diffusion tensor imaging (DTI), and intravoxel incoherent motion (IVIM). Diffusion tensor parameters (mean diffusivity [MD] and fractional anisotropy [FA]) were obtained by iterative weighted linear least squares fitting of the DTI data and mono-, bi-, and triexponential fit parameters (D_1, D_2, D_3, f_{fast2}, f_{fast3}, and f_{interm}) using a nonlinear fit of the IVIM data. Average parameters were calculated for three regions of interest (ROIs) (cortex, medulla, and rest) and from fiber tractography. Goodness of fit was assessed with adjusted R^2 (R^2_{adj}) and the Shapiro-Wilk test was used to test residuals for normality. Maps of diffusion parameters were also visually compared.
Results: Fitting the diffusion signal was feasible for all models. The three-component model was best able to describe fast signal decay at low b values ($b < 50$), which was most apparent in R^2_{adj} of the ROI containing high diffusion signals (ROI_{rest}), which was 0.42 ± 0.14, 0.61 ± 0.11, 0.77 ± 0.09, and 0.81 ± 0.08 for DTI, one-, two-, and three-component models, respectively, and in visual comparison of the fitted and measured S_0. None of the models showed significant differences ($P > 0.05$) between the diffusion constant of the medulla and cortex, whereas the f_{fast} component of the two and three-component models were significantly different ($P < 0.001$).
Conclusion: Triexponential fitting is feasible for the diffusion signal in the kidney, and provides additional information.
Level of Evidence: 2
Technical Efficacy: Stage 1

J. MAGN. RESON. IMAGING 2017;46:228–239

Diffusion magnetic resonance imaging (MRI) of the kidney is a growing field of research, as it allows assessment of tissue characteristics. The method makes no use of ionizing radiation and does not require extraneous contrast agents that might impede kidney function. Research has shown that it is feasible to differentiate between different renal tissue types (ie, cortical and medullar tissues) using diffusion tensor imaging (DTI) MRI-derived parameters such as mean diffusivity (MD)—quantifying the magnitude of diffusion—and fractional anisotropy (FA)—a measure for diffusion anisotropy.[1,2] Several studies have demonstrated that in healthy subjects the cortical MD is higher than the MD in the medulla, whereas cortical FA is lower than medullar FA.[3–10] The higher diffusion anisotropy is usually attributed to the radial organization of tubules and vasculature in the renal pyramids.[1,4–9,11] In addition, it has been shown that it is possible to differentiate between healthy and diseased tissue using diffusion tensor MRI parameters MD and FA, for example, in follow-up of kidney transplants[12,13] and in the early detection of diabetic nephropathy.[14]

View this article online at wileyonlinelibrary.com. DOI: 10.1002/jmri.25519

Received Aug 18, 2016, Accepted for publication Oct 7, 2016.

*Address reprint requests to: S.v.B., University of Twente, Postbus 217, 7500 AE Enschede, The Netherlands. E-mail: s.j.vanbaalen@utwente.nl

From the [1]MIRA Institute for Biomedical Technology and Technical Medicine, University of Twente, Enschede, The Netherlands; [2]Image Sciences Institute, University Medical Center Utrecht, Utrecht, The Netherlands; [3]Department of Pediatric Urology, Wilhelmina Children's Hospital, UMC Utrecht, Utrecht, The Netherlands; [4]Department of Pediatric Nephrology, Wilhelmina Children's Hospital, UMC Utrecht, Utrecht, The Netherlands; and [5]Department of Radiology, University Medical Center Utrecht, Utrecht, The Netherlands

Additional supporting information may be found in the online version of this article

In addition to the microscopic motion of water in tissue, diffusion MRI is also sensitive to processes such as vascular perfusion and tubular flow.[15] Because the signal attenuation due to perfusion is much greater than attenuation caused by diffusion, both signals can be separated by using a two-component intravoxel incoherent motion (IVIM) model. This is done by fitting of the diffusion signal decay over a range of b-values to a biexponential function, in which the fast signal decay at lower b-values ($b < 200$) is attributed to fast water movement processes, "pseudodiffusion," and the decay at higher b-values to hindered diffusion.[15] The two-component model was shown to be a better fit to the diffusion signal in the kidney than the one-compartment models.[16] Several studies showed IVIM parameters to be sensitive to pathological processes in the kidney, such as allograft rejection,[17] renal tumors,[18,19] renal artery stenosis,[20] renal dysfunction,[21] cortical defects,[22] and vesicoureteral reflux.[23]

However, there is great variability between the obtained values for diffusion D, pseudodiffusion D^*, and pseudodiffusion signal fraction f. These differences are in part a consequence of the use of different acquisition or processing protocols, for example, the b-values used,[9,24] or of using different fitting algorithms.[3,25] However, there might also be physiological causes for this variability; for example, pseudodiffusion was found to correlate with perfusion in an electrocardiogram (ECG)-triggered time-resolved study of healthy kidneys,[26] while IVIM-derived parameters were also shown to be sensitive to diuretic challenges.[27] This has led to the belief that pseudodiffusion in the kidney consists of a perfusion and a tubular, or free water flow, component.[3,28]

Therefore, we propose a three-component model for the diffusion signal in the kidney, to account for a pure diffusion, an ultrafast, and an intermediate component.[29] A three-component model has been applied in other abdominal organs, ie, the liver[30,31] and the prostate,[32] where the intermediate component was believed to reflect free diffusion[31,32] or microperfusion.[30]

In this study we compare the three-component model for the diffusion signal in healthy human kidneys with commonly used models, ie, DTI and IVIM. The purpose was to evaluate if the three-component model correctly describes the signal and whether it can provide complementary anatomical or physiological information about the underlying kidney tissue.

Materials and Methods

Subjects

Local Institutional Review Board approval was obtained for this study and written informed consent was given prior to the MRI examination. Ten healthy volunteers with no previous history of kidney disease were included. Subjects were not given any restrictions regarding fluid or food intake.

MRI Acquisition

Volunteers were examined on a 3T MR clinical scanner (Philips, Achieva, Philips Healthcare, Best, The Netherlands), using a 16-element body coil (SENSE XL Torso coil). Volunteers underwent coronal T_2-weighted anatomical imaging and diffusion weighted imaging (DWI), which consisted of two scans: a DTI scan with $b = 0$, 100, and 300 s/mm^2 in 15 gradient directions, and an IVIM scan with $b = 10$, 25, 40, 75, 100, 200, 300, 500, 700 s/mm^2 in three gradient directions. All image acquisitions were navigation-triggered[7,10,33] (see Table 1 for the MRI acquisition details). After acquisition, all raw images were assessed for data quality. Images were evaluated by the principle investigator (S.v.B., 1 year of experience) in agreement with experienced MRI scientists (A.L. and M.F., 10 years of experience) and an experienced pediatric urologist (P.D., 25 years of experience) on a three-point scale (1 = bad, 2 = sufficient, 3 = good) for the presence of visible blurring, signal dropouts, susceptibility artifacts, and distortions. Datasets with a score of 2 or 3 were considered of adequate quality for further processing.

Image Preprocessing

All preprocessing was performed with DTITools[34] and "ExploreDTI"[35] and were comprised of the following steps. First, because of differences in the motion of the left and right kidneys, the data were cropped in two separate datasets, containing the left and right kidney, respectively, which were processed independently. Next, all DWI data were corrected for motion due to breathing and eddy current-induced deformations by a two-step registration process. First, all diffusion-weighted images were registered to the unweighted images[10,33] using a nonrigid 2D b-spline (Elastix[36,37] registration algorithm, aligning the slices within the diffusion-weighted volumes as well as the volumes to each other and the unweighted volume. Second, these motion-corrected data were registered to the T_2-weighted anatomical images, using an 3D affine registration algorithm. At each step, the B-matrix was adjusted to take any rotational components into account.[38] In order to obtain corresponding resolutions, the diffusion-weighted data and the anatomical images were resampled to 2 mm isotropic resolution. To segment the kidney volume from the background, masks were obtained by manually drawing regions of interest (ROIs) around the kidney in the sagittal slices of the T_2-weighted TSE scans using ITK snap (www.itksnap.org[39]).

Data Analysis

To obtain diffusion parameters the corrected DTI and IVIM datasets were analyzed with four different methods, ie, DTI and mono-, bi-, and triexponential fitting (see Table 2). Diffusion tensors were computed from the DTI data using an iterative weighted linear least squares (iWLLS) algorithm with outlier rejection,[40,41] after which the FA and MD were calculated for each voxel. The IVIM data were processed using three different isotropic diffusion decay models, ie, with one, two, and three diffusion components. The single-component model is expected to be most similar to the MD obtained from the tensor model, as the tensor model is also monoexponential. The two-component model (the IVIM model) has been used before in diffusion imaging of the kidney and allows one to separate the fast (pseudo)diffusion of urine and blood from the slower tissue diffusion. The three-component model allows for both a fast and intermediate diffusion component in addition to the slower tissue diffusion. Mono-, bi-, and triexponential models were fitted using a nonlinear least squares method (Levenberg-

TABLE 1. MRI Acquisition Details

Sequence	T2-TSE	DTI	IVIM
Respiratory correction	Trigger	Trigger	Trigger
Scan time per respiration	0:02.04	0:01.3	0:01.3
Acquisition plane	Coronal	Coronal	Coronal
Field of view	450x450	336x204	336x204
TSE factor	20	—	—
TR/TE (msec)	2418/100	1267/39	1344/45
Startup echoes	0	—	—
b-value (s/mm^2)	—	0, 100, 300	0, 10, 25, 40, 75, 100, 200, 300, 500, 700
Flip angle (deg)	90	—	
Gradient directions	—	15	3
EPI factor (ETL)	—	55	55
SENSE factor	4	1.5	1.5
Acquisition matrix	400×320	112×68	112×68
Acquisition voxel size (mm^3)	1.13 × 1.41 × 3.0	3.0 × 3.0 × 3.0	3.0 × 3.0 × 3.0
Half Fourier scan factor	—	0.655	0.655
Slice thickness/gap (mm)	3.0 /-	3.0/-	3.0/-
Number of slices	25	30	30
Number of averages	6	3 (b=0, 12)	2 (b=0, 8)
Type of fat suppression	No	SPIR	SPIR
Total acquisition time (min)	4:03.0	10:18.0	06:54.0

Marquardt). For the two- and three-component models the models were first fitted to the average signals from the whole kidney volume to obtain values for D_{fast2}, D_{interm}, and D_{fast3}. Next, with D_{fast2}, D_{interm}, and D_{fast3} fixed to the average value of all kidneys of all subjects the voxel wise fit for S_0, D_1,D_2,D_3, f_{interm}, f_{fast2}, and f_{fast3} was performed. These voxelwise fits result in maps that were used for visual comparison: fitted S_0 was compared to the measured S_0 for each model, the diffusion D_1,D_2,D_3 were compared to each other and the fraction maps for the two- and three-component fits were compared to each other and to the anatomical T_2 maps to analyze the relation to anatomical structures.

ROI Selection

ROIs selecting the cortex, medullae, and the rest of the kidney (which includes the pyelum, large renal vessels, and other high-signal regions) were defined using an automated algorithm. First, after smoothing the maps with a Gaussian kernel with a radius of two voxels, masks were computed by selecting all regions that had

TABLE 2. Signal Equations for the DTI Model and the One-, Two-, and Three-Component Models

Model	Equation	
DTI	$S_b = S_0 e^{-b\vec{g}D\vec{g}}$	[1]
IVIM$_1$	$S_b = S_0{}^{-bD_1}$	[2]
IVIM$_2$	$S_b = S_0\left((1-f_{fast,2})e^{-bD_2} + f_{fast,2}e^{-bD_{fast,2}}\right)$	[3]
IVIM$_3$	$S_b = S_0\left((1-f_{interm.}-f_{fast,3})e^{-bD_3} + f_{interm.}e^{-bD_{interm.}} + f_{fast,3}e^{-bD_{fast,3}}\right)$	[4]

S_0 is the unweighted signal; S_b is the diffusion weighted signal; b is the b-value; $\vec{g}$ is the gradient direction; D the diffusion tensor; D_1,D_2, and D_3 the diffusion constants obtained from the one-, two-, and three-component IVIM models, respectively; $D_{fast,2}$ and $D_{fast,3}$ the fast diffusion constants from the two- and three-component model, respectively; D_{interm} the intermediate diffusion constant from the three-component model; $f_{fast,2}$,f_{interm} and $f_{fast,3}$ the signal fractions of the $D_{fast,2}$, D_{interm}, $D_{fast,3}$ component.

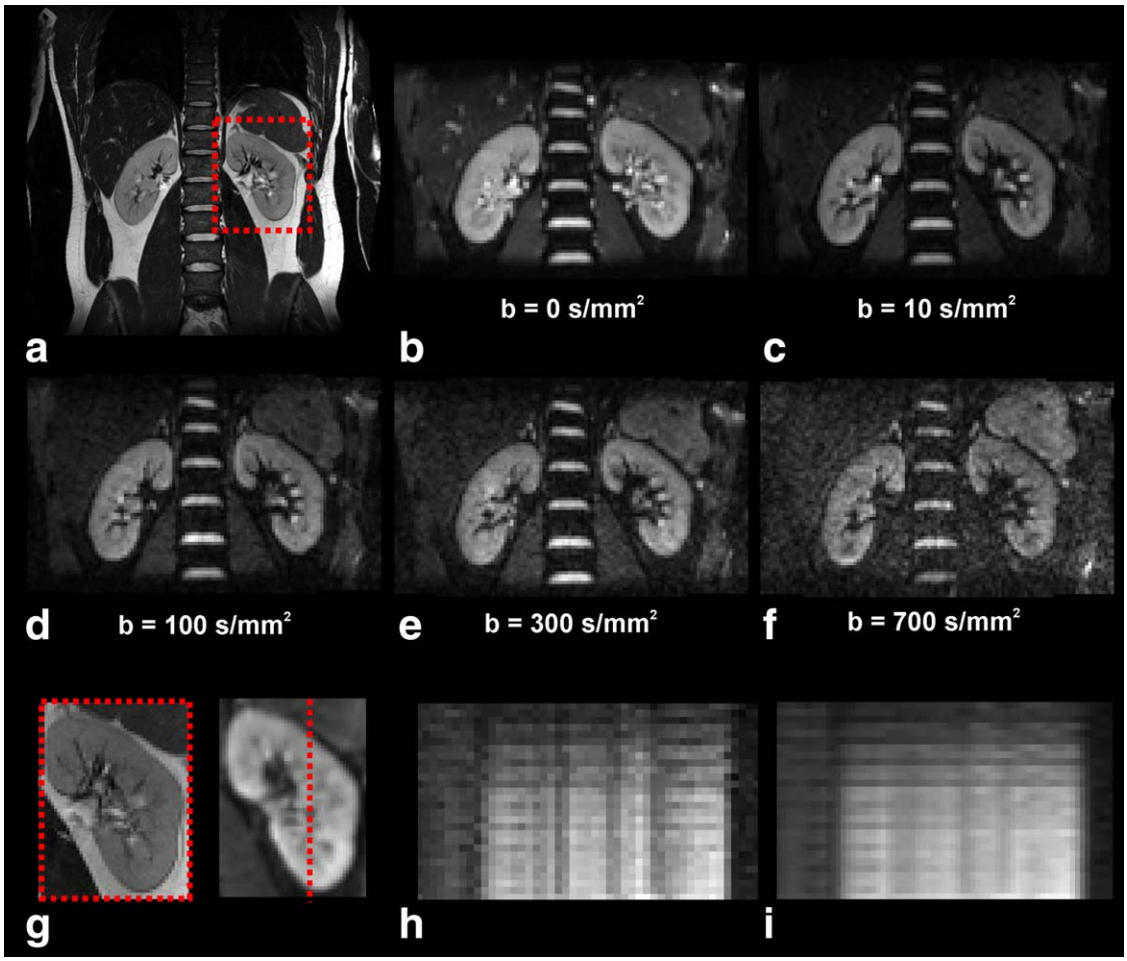

FIGURE 1: Unprocessed data, the cropped data, and effect of registration. A: T_2-weighted anatomical image of both kidneys. The red square indicates the cropped area to select a single kidney (G). B–F: Diffusion-weighted images for *b*-value of 0, 10, 100, 300, and 700 s/mm^2, respectively. G: Cropped kidney (left T_2-weighted, right diffusion-weighted image after registration), the vertical red dashed line in the diffusion-weighted image indicates the cross-section shown in H,I. H,I: Cross-section of diffusion-weighted images before (H) and after (I) registration.

an MD (DTI model) and an D_1 (monoexponential model) greater than 5.0 mm^2/s (faster than free water at 37°), and defined as the ROI containing "the rest," ie, ROI_{rest}. Next, the mask that was drawn manually to segment the kidney (see section Image Preprocessing) was eroded by three voxels. This eroded mask and the ROI_{rest} were subtracted from the manual mask to obtain the ROI that contained the cortex, ROI_{cortex}. Finally, the $ROI_{medulla}$ was defined by subtracting the ROI_{cortex} and the ROI_{rest} from the manually drawn mask of the kidney.

In addition to ROI-based analysis, tractography-based analysis was performed. Whole volume fiber tracts were generated from the tensors obtained from the DTI data with a seeding distance of $2 \times 2 \times 2$ mm^3. Tractography was allowed in voxels with an FA between 0.05 and 0.9 and an MD between 0.1 and 5.0 mm^2/s and was terminated if tracts changed more than 20 degrees per 1-mm step. From the whole volume fiber tractography results, tract density (TD) maps were generated (amount of tracts per voxel).[42] To segment renal pyramids, regions with a high tract density were selected from the tract density map: knowing that tubules and collecting ducts congregate in papillae, papillae were segmented by selecting regions that had a TD higher than 10% of the mean TD of the kidney. The tract density threshold was established experimentally, balancing between optimally selecting papillae and eliminating spurious tracts.

Statistical Analysis

The goodness of fit of the mono-, bi-, and triexponential signal decay models as well as the DTI model was assessed by analysis of the model residuals. First, the adjusted R^2 (R^2_{adj}) was calculated, where a high value of R^2_{adj} indicated that the model describes the data appropriately. Second, the residuals were tested for normality using the Shapiro-Wilk test. If the residuals have a normal distribution the test parameter W will converge to the value of 1 and the P-value is greater than 0.05.

The diffusion parameters, signal fractions, W and R^2_{adj} were calculated per ROI (ie, cortex, medulla, and rest) as well as for the tract volume. Differences between the regions were evaluated using analysis of variance (ANOVA) analysis and corrected for multiple comparisons using a Bonferroni post-hoc test. Values were considered different if the P-value of the post-hoc test was smaller than 0.05. For W, only voxels that had a P-value greater than 0.05 were used in the ROI analysis and the percentage of rejected voxels was calculated.

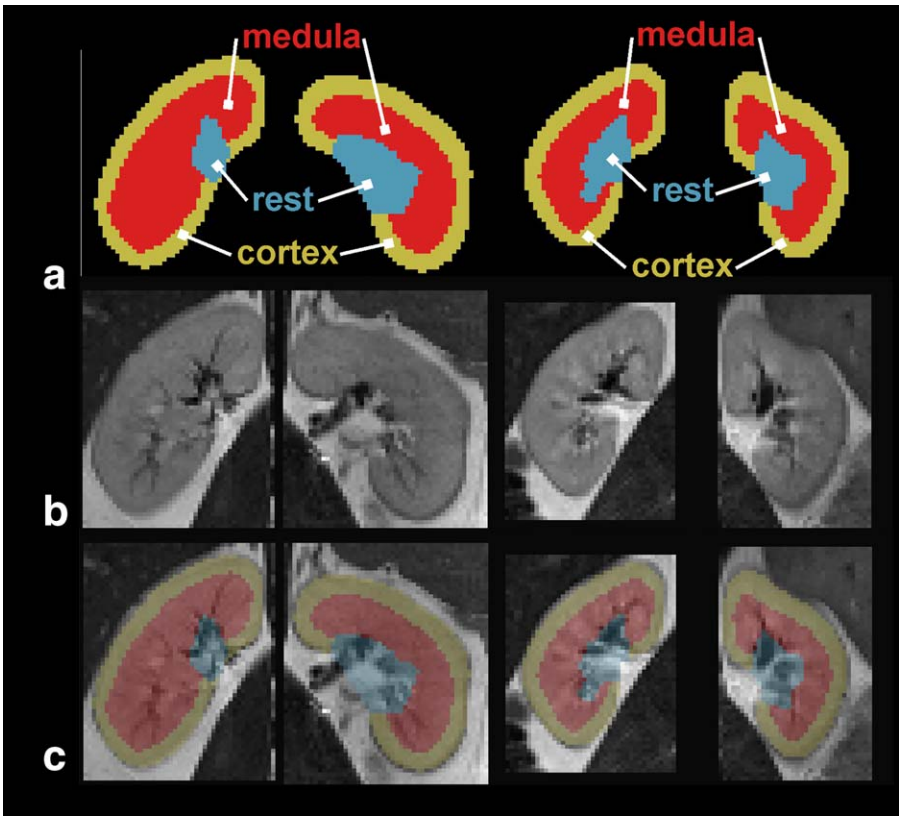

FIGURE 2: Automatically generated mask for selecting the regions of interest, ie, cortex (yellow), medulla (red), and rest (blue). A: Masks for two subjects. B: T_2-weighted anatomical images. C: Masks overlaid on the anatomical images.

The correlations between FA and signal fractions were investigated using a Spearman's rank test. If the parameters are correlated the test parameters will converge to one. The correlation was considered significant if the *P*-value was smaller than 0.05.

Results

Subjects

All volunteers (three males, seven females; ages 28.2 ± 9.5; range 23–55 years old) were successfully scanned. After examination of the scans by a radiologist, one kidney was excluded from further analysis because of a cyst, and for one dataset the IVIM data were lost, leaving 19 kidneys for DTI analysis and 17 for IVIM analysis.

MRI Acquisition and Image Preprocessing

All acquired datasets had sufficient data quality (four scans in category 2 and 15 scans in category 3, out of 10 DTI scans and 9 IVIM scans) and could be used for further analysis. An example of the T_2, DTI, and IVIM data is shown in Fig. 1A–F. After each kidney was cropped into a separate dataset (Fig. 1G) the diffusion data were registered to correct for residual breathing motion (Fig. 1H,I). Figure 2 shows the automatic selection of the three ROIs selecting the cortex, medulla, and rest, based on the manually drawn whole kidney mask.

Data Analysis

Figure 3 shows mono-, bi-, and triexponential fits of the whole volume. The signal averaged over the whole kidney volume as a function of *b*-values for all kidneys of all subjects are plotted separately in one graph for the one-, two-, and three-component models in the left column of Fig. 3A. Theses plots show almost identical relations between b-value and average signal for each kidney. Therefore, the signal from all kidneys were taken together and averaged to obtain the values for D_{fast2}, D_{interm}, and D_{fast3}, which is demonstrated in Fig. 3A in the right column. These values fitted from the average data of all kidneys were used for a voxel wise fit for S_0, D_1,D_2,D_3, f_{interm}, f_{fast2}, and f_{fast3}. Comparing the maps of the fitted S_0 to the measured S_0 suggests that the mono- and biexponential fits were not able to accurately fit S_0, especially in the regions with a high diffusion signal (white arrow, Fig. 3B, left two columns). Furthermore, the diffusivity found with the mono- and biexponential fits (D_1 and D_2) are similar but higher than that of the triexponential fit (D_3).

Considering the consecutive images for all b-values in Fig. 4A, the three-component model allows one to differentiate between the fast signal decay occurring between $b = 0$ and $b = 10$ s/mm^2 and the intermediate signal decay occurring between $b = 10$ and $b = 200$ s/mm^2. For example, in the images for $b = 0$ s/mm^2 the signal from fast-flowing

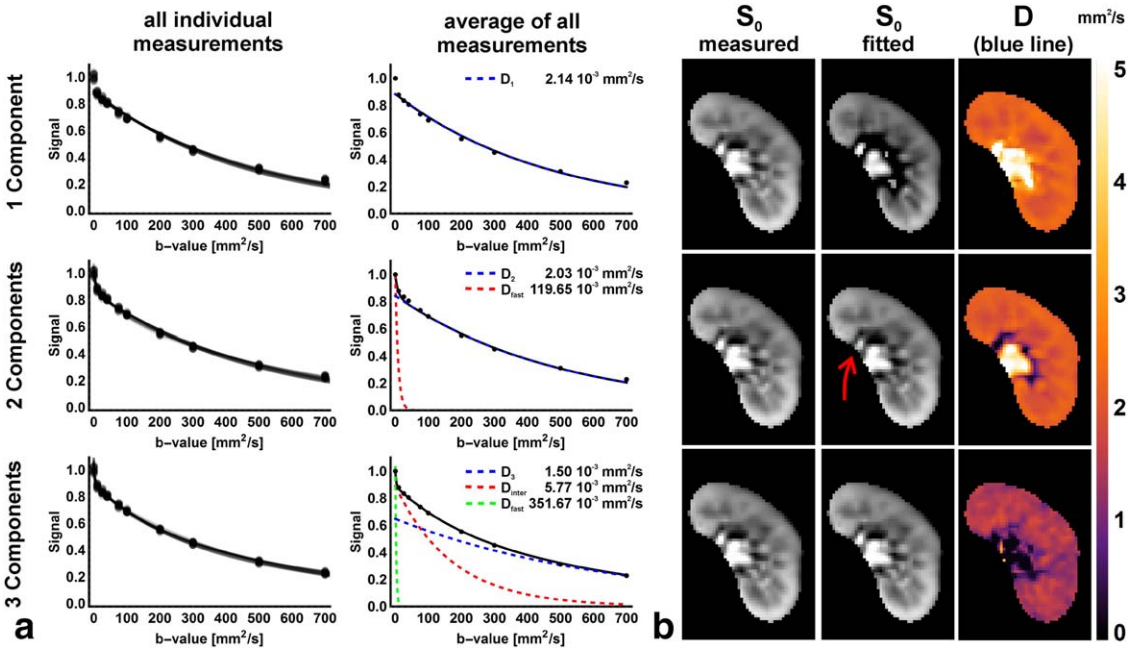

FIGURE 3: Fits of the whole kidney volume signal using mono-, bi-, and triexponential IVIM fits and the fitted S_0 and D maps. A: The whole volume diffusion-weighted signal as a function of b-value with the corresponding model fits. The left column shows all the data and fits of the individual subjects and kidneys ($n = 17$). The right column shows the average signal of all subjects and kidneys together with the models fits and its individual components. B: The measured unweighted signal S_0 together with the fitted S_0 and D. Both the one- and two-component models are unable to correctly describe the signal attenuation resulting in an underestimation of S_0. For the two-component model this is only apparent in the bright signals, as indicated by the red arrow. The estimated diffusion becomes lower with increasing components in the IVIM model.

water in renal arteries is visible, but it is completely absent in $b = 10$ s/mm^2. The signal from free water in the pyelum is visible in all maps up to $b = 200$ s/mm^2. In the two-compartment model, this last process with an intermediate decay rate and its corresponding structure (the pyelum) is added to the slow diffusion compartment and visualized in the 1-f_{fast2} fraction map in the two-compartment model. As demonstrated in Fig. 4B, the two-, and three-component models show a very similar signal fraction of the fast diffusion component f_{fast2} and f_{fast3}. However, the three-component model allows for an additional intermediate diffusion signal fraction $f_{fastinterm}$. This allows for the visualization of complementary structures, such as the kidney pyelum, the cortex, and renal columns in the intermediate compartment. The complementarity of the fraction maps is visualized in Fig. 4C, which shows the three signal fractions of the three-component model as RGB maps next to the anatomical T_2-weighted image. For all the imaged kidneys, a similar pattern is found (see Fig. 4D) in which f_{fast3} mostly corresponds to the renal arteries and veins, f_{interm} mostly corresponds with the renal cortex, renal columns, and renal pelvis, and $f_{1\text{-}interm\text{-}fast}$ reflects kidney parenchyma.

DTI analysis and fiber tractography was feasible in all kidneys. A TD map of whole volume tractography is shown in Fig. 5A. The regions with high tract density that were used to select the fiber tracts are shown in Fig. 5B. The resulting fiber tracts that only belong to the renal pyramids are shown in Fig. 5C. Figure D–F show the direction color coded FA map, direction color encoded fiber tracts, and MD color encoded fiber tract, respectively. Regions that allow fiber tractography showed very uniform FA and MD. Furthermore, the fiber tracts also have in general very uniform signal fractions as obtained from the three component IVIM model, as shown in Fig. 5G–I.

Statistical Analysis

Values of R^2_{adj} for the DTI and the mono-, bi-, and triexponential fits of one kidney are shown in Fig. 6B and average values for all ROIs and tracts of all kidneys are given in Table 3 and all P-values for differences between ROIs are also given in the Supplementary Table. Highest and most homogeneous values for R^2_{adj} were obtained using the three-component model and lowest values were obtained using the DTI model (see Table 3). The two-component model showed similar values for R^2_{adj} with the exception of those obtained in the rest ROI and those obtained from the tracts. For the cortex the mono-, bi-, and triexponential models performed similarly.

The test statistics of the Shapiro-Wilk test of one kidney are shown in Fig. 6C and the average values of the percentage of voxels with a $P < 0.05$ for all ROIs and tracts of all kidneys are given in Table 3. The highest percentage of voxels with normally distributed residuals were obtained using the three-component model. The two- and three-

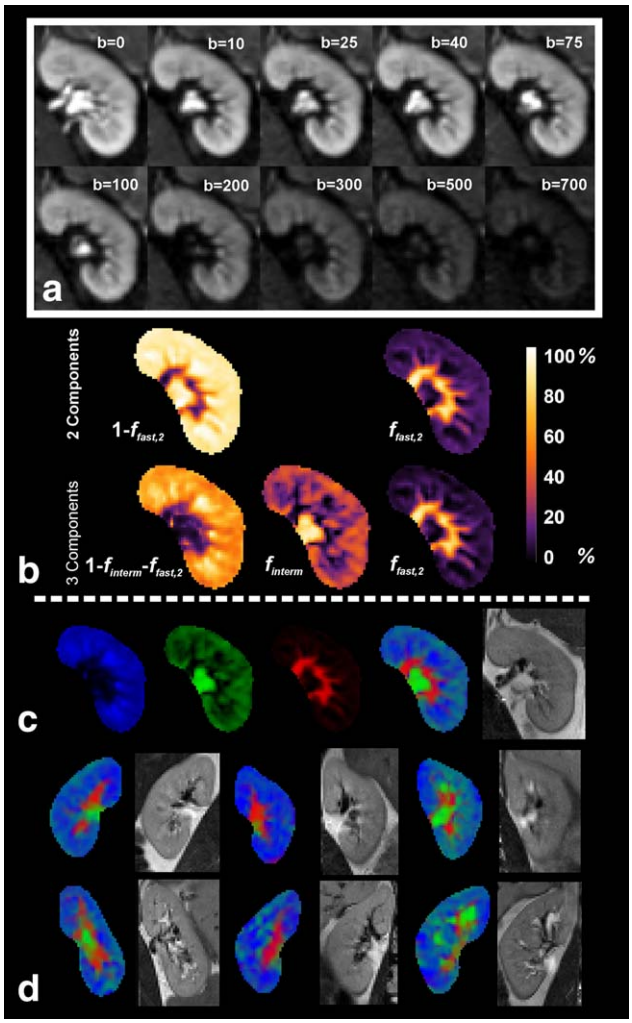

FIGURE 4: Signal fraction maps resulting from the bi-, and triexponential IVIM fits. A: Diffusion-weighted IVIM data for *b*-values 0 to 700 s/mm^2. B: Signal fraction maps in percentage for the bi- and triexponential IVIM fits. C: Merged signal fraction maps of the triexponential IVIM fit color coded as red green and blue for the $1\text{-}f_{interm}\text{-}f_{fast2}$, f_{interm}, and f_{fast2}, respectively, next to the anatomical T_2-weighted images. It is apparent that f_{interm} and f_{fast2} correspond well to the urine and blood in the anatomical images, respectively.

component models showed similar results in the cortex and medulla, whereas the one-component model had a much lower percentage of voxels with normally distributed residuals in the medulla. Furthermore, the DTI model had a lower percentage of voxels with normally distributed residuals compared to the mono-, bi-, and triexponential models with the exception of the rest ROI and the medulla in the single-component model.

Average parameter values from the DTI and mono-, bi-, and triexponential fits for all ROIs and tracts are given in Table 3 and all *P*-values for differences between ROIs are also given in the Supplementary Table. The FA in the ROI_{cortex} was significantly lower than in the tracts and ROI_{rest}. Furthermore, the FA was the only parameter that differed significantly between the $ROI_{medulla}$ and the tracts, where the medulla had a significantly lower FA. The MD and the diffusion constants from the one-, two-, and three-component models (ie, D_1, D_2, and D_3, respectively) all showed significant differences between the ROI_{rest} and the ROI_{cortex}, $ROI_{medulla}$, and tracts. These values were not significantly different between the ROI_{cortex} and $ROI_{medulla}$ ($P = 1$, $P = 1$, $P = 0.363$, and $P = 1$, respectively). The MD was higher than D_1, D_2, and D_3. Additionally, with increasing components in the signal decay models the values for D decreased. The signal fractions f_{fast2} and f_{fast3} showed significant differences between all ROIs and tracts with the exception of the $ROI_{medulla}$ and the tracts ($P = 0.762$ and $P = 1.000$). The signal fraction f_{interm} was only significantly different between the ROI_{rest} and the $ROI_{medulla}$ and tracts.

Figure 7 shows the correlation between the average values of FA and the signal fractions f_{fast2}, f_{interm}, and f_{fast3} for all ROIs of all kidneys. Both f_{fast2} and f_{fast3} showed a significant ($P < 0.001$) and high correlation with FA from the DTI model, 0.751 and 0.756, respectively.

Discussion

We compared a three-component model for the diffusion signal in healthy human kidneys with commonly used models, ie, DTI and IVIM using the whole volume signal and voxelwise fits allowing ROI-based analysis. In addition, visual assessment was also performed to assess consistency and complementarity of the different diffusion metrics. For all automatically generated ROIs the three-component fit had the lowest R^2_{adj} and the highest percentage of voxels with normally distributed residuals. Additionally, we showed that the f_{fast2} and f_{fast3} from the two- and three-component models showed a high and significant correlation with FA from the DTI model. DTI and IVIM are well-established fitting methods that have been applied in numerous diffusion MRI studies of the kidneys with consistent results,[5–9,11,16,26–28,33,43] which are in line with our results.

The diffusion coefficient (MD for DTI, D_1, D_2, and D_3 for mono-, bi-, or triexponential fitting, respectively) decreases when more components are used, suggesting that the diffusion signal of the kidney partly includes a signal fraction that originates from fast-moving water instead of normal diffusion. IVIM fitting can differentiate between slow and fast-moving water, as was put forward by earlier IVIM studies in the kidneys.[15,16,20,21,24,26–28] With the triexponential fit, the diffusion coefficient further decreases, suggesting that biexponential fitting does not fully differentiate between pure diffusion and other water motion processes and that introducing an additional intermediate component allows to further distinguish between them. The value of D_3 is more in range of MD values found in other organs such as muscle,[44] heart,[45] and brain.[46]

Considering the goodness of fit for all diffusion models, the bi- and triexponential models result in lower

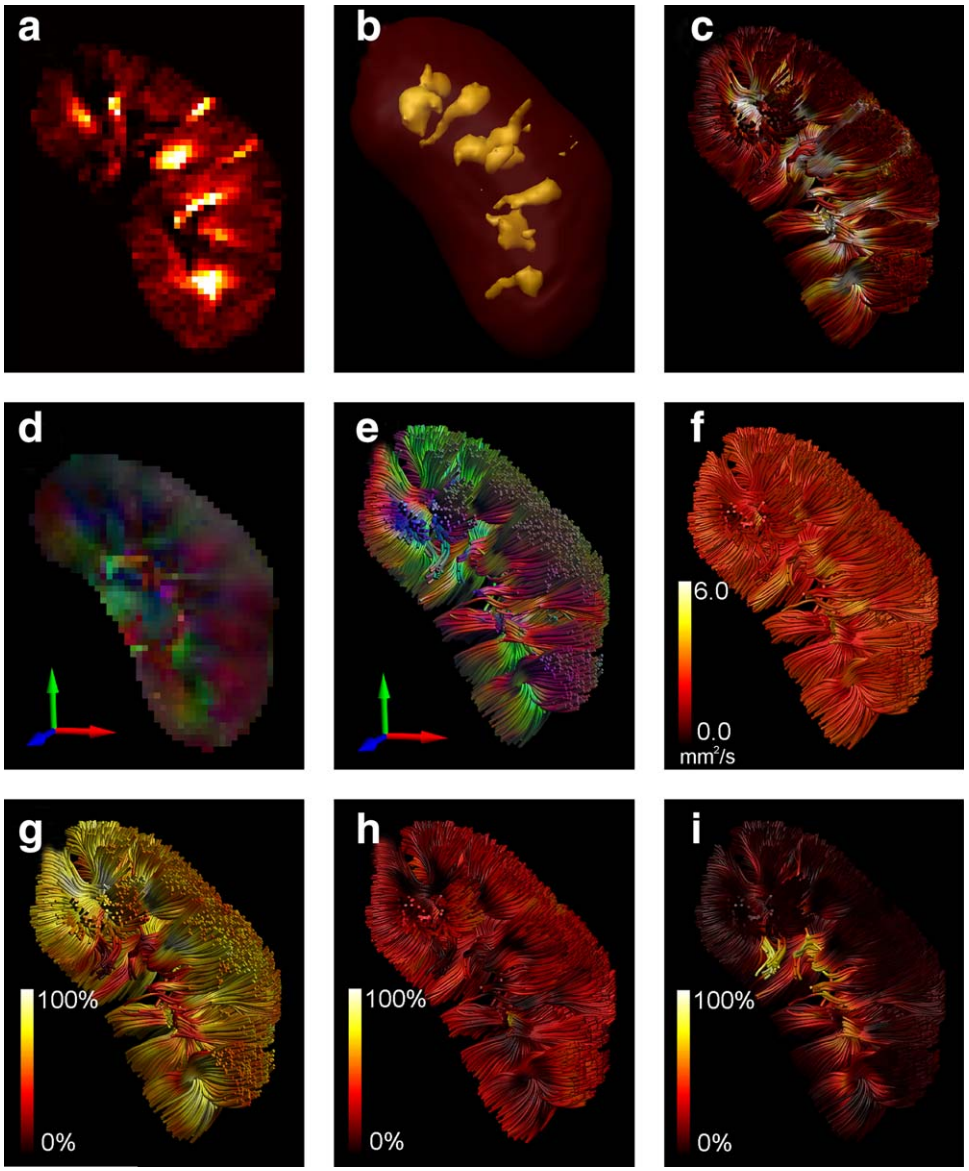

FIGURE 5: Fiber tracts and tract selection from the DTI model color coded for diffusion parameters and signal fractions. A: Tract density map from whole volume fiber tractography. B: Tract selection regions generated from the tract density map, where the tract density is greater than 10% of the average tract density. C: Fiber tracts selected with the tract density regions, color coded for the tract density. D: Color coded FA map. E: Fiber tracts color coded for FA and direction as indicated by the red green and blue arrows. F: Fiber tracts color coded for MD. G–I: Fiber tracts color coded for the signal fractions of the three-component IVIM model.

residuals than a one-compartment (monoexponential and DTI) model. This is in line with an earlier study in which Wittsack et al have shown that the IVIM model is preferred over monoexponential models for fitting the diffusion signal in the kidney.[16] In the ROI_{rest} fast-moving water is located, for example, within the renal vessels and the pyelum. The three-component model seems better equipped to handle these regions than the IVIM model, resulting in a higher R^2_{adj} and normally distributed residuals, although the differences between the two- and three-component models are not statistically significant and might be attributed to overfitting because of a higher number of parameters. The goodness of fit for the renal parenchyma is similar for the IVIM and three-component model, but these regions may also contain vessels or other structures containing both fast and intermediate water motion processes that cannot be accurately modeled using a biexponential fit. Therefore, we propose that using a triexponential signal decay fit provides more information on the component of the signal that is associated with intermediate diffusion rate, in the order of magnitude of free water. Our findings agree with earlier application of triexponential fits to the liver and the prostate, where the additional component is believed to correspond with free water[37,38] or microperfusion.[36]

Assessment of the fits demonstrates the plausibility of an additional, intermediate component, especially the

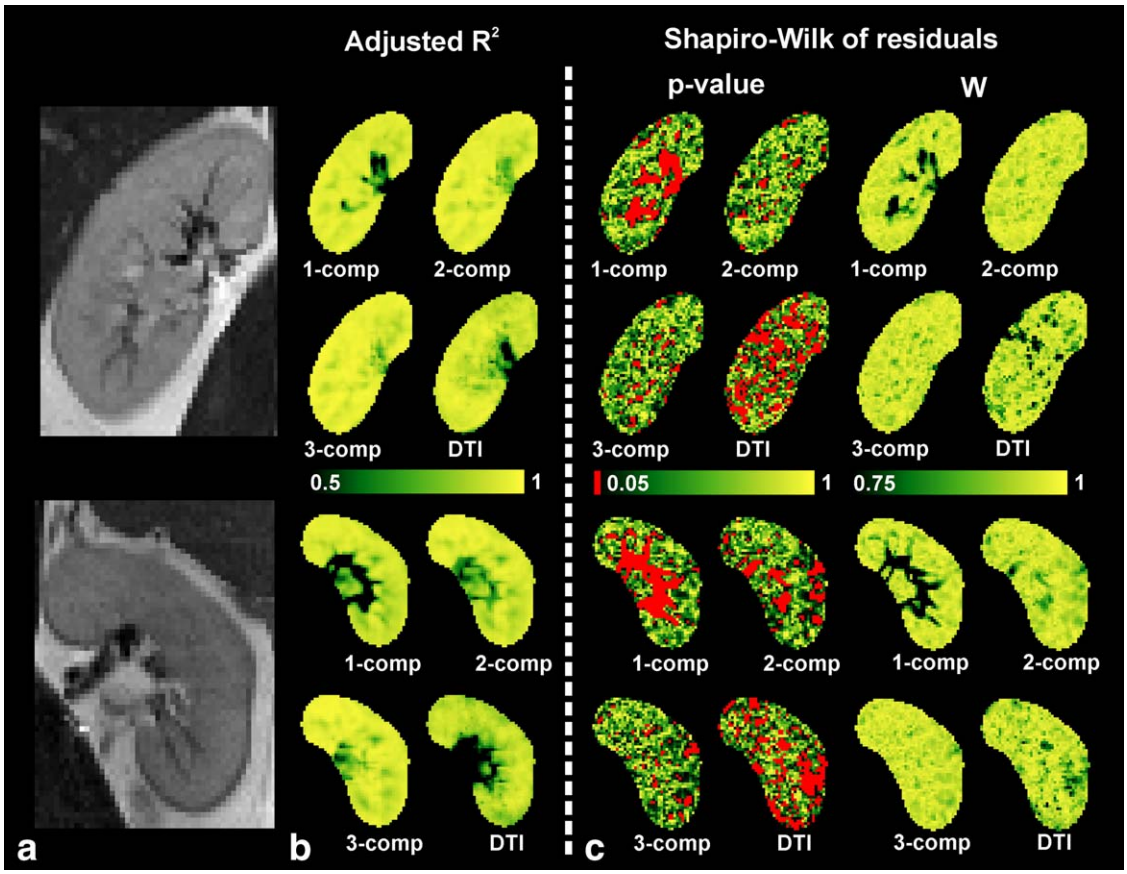

FIGURE 6: R^2_{adj} maps and test statistics from Shapiro-Wilk test. **A:** The anatomical T_2-weighted images of the left and right kidney. **B:** The voxelwise R^2_{adj} values for the DTI and mono-, bi-, and triexponential IVIM fits. **C:** The voxelwise *P*-values and *W* from the Shapiro-Wilk test. *P*-values < 0.05 are color coded red.

intermediate *b*-value regions ($10 < b < 300$ s/mm^2) but also $b = 700$ s/mm^2 are better described with the three-component model. Comparing the measured S_0 to the fitted S_0 suggests that the triexponential fit is more accurate than the monoexponential fit as well as the biexponential fit. Especially at those regions where fast-moving water is expected (outside of the kidney parenchym), which is also demonstrated by the R^2_{adj} maps and Shapiro-Wilk residual maps. In a two-component model, the conventional IVIM model is a more suitable fit for the diffusion signal in the kidney parenchyma than monoexponential models. Areas with fast water motion, such as blood flow in large vessels, are more accurately fitted with a three-component model.

In the cortex and medulla the pattern of D_1, D_2, and D_3 also changes with increasing model components. In the D_1 and D_2 maps, high values are found in the cortex and the renal columns between the renal pyramids. Using a three-component model this pattern in the D_3 maps disappears and is almost completely described by the intermediate diffusion constant D_{interm} and the its corresponding signal fraction f_{interm}.

Comparing the signal fraction maps with T_2 images suggests that the intermediate component reflects free water, which is predominantly found in the pyelum, where urine is collected after filtering in the nephron. In comparison to T_2 images, the fast component reflects blood flow, which is predominantly found in the large vessels. In the renal parenchyma it is more difficult to pinpoint the structure or physiological process to which the signal fractions refer by comparing to the T_2 images. Flow of blood and urine in the nephrons and collecting ducts in the same order of magnitude within one voxel cannot be distinguished. Adding an intermediate component affects the diffusion fraction ($1\text{-}f_{fast2}$ for the biexponential fit and $1\text{-}f_{interm}\text{-}f_{fast3}$ for the triexponential fit) map: in the biexponential fit this map is largely homogeneous in the renal parenchyma, whereas in the triexponential fit a pattern that reflects the pyramidal structure in the renal parenchyma is visible. This corresponds to the observations in the changes in D as a result of adding additional components described above. These observations suggest that fraction maps derived from triexponential fitting provide additional information on structures associated with intermediate water flow processes. These findings may be employed in the development of imaging tools that aid in the diagnosis of patients with renal pathologies that alter physiologic water motion processes, such as renal artery stenosis, chronic parenchymal disease, or renal lesions such as scarring, cysts, or tumors.

TABLE 3. R^2_{adj}, Percent Of Voxels With $P < 0.05$ From the Shapiro-Wilk Test, and DTI and Mono-, Bi-, and Triexponential Fitting Parameters for Each ROI and Track Volume

		Cortex	Medulla	Rest	Tracts	
R^2_{adj}	DTI	0.80 ± 0.10	0.76 ± 0.09	0.42 ± 0.14	0.70 ± 0.11	*b, d, f*
	1-comp	0.91 ± 0.03	0.87 ± 0.03	0.61 ± 0.11	0.82 ± 0.07	*b, d, f*
	2-comp	0.92 ± 0.03	0.91 ± 0.03	0.77 ± 0.09	0.87 ± 0.05	*b, d, f*
	3-comp	0.92 ± 0.03	0.91 ± 0.03	0.81 ± 0.08	0.89 ± 0.04	*b, d, f*
% voxels S-W test with $P < 0.05$	DTI	28.40 ± 8.94	27.30 ± 9.61	24.50 ± 5.34	27.20 ± 10.10	
	1-comp	20.10 ± 12.40	32.00 ± 11.70	53.00 ± 14.40	29.80 ± 12.00	*a, b, d, f*
	2-comp	20.80 ± 12.60	16.30 ± 9.17	28.50 ± 11.50	16.90 ± 9.39	*d, f*
	3-comp	20.10 ± 11.90	16.70 ± 8.83	25.00 ± 10.80	17.80 ± 9.17	
DTI	FA	0.22 ± 0.04	0.23 ± 0.03	0.28 ± 0.03	0.28 ± 0.03	*b, c, d, e*
	MD [10^{-3} mm^2/s]	2.17 ± 0.10	2.11 ± 0.11	2.52 ± 0.25	2.14 ± 0.13	*b, d, f*
1-comp	D_1 [10^{-3} mm^2/s]	2.12 ± 0.09	2.09 ± 0.11	5.52 ± 3.84	2.32 ± 0.32	*b, d, f*
2-comp	$f_{fast,2}$ [%]	9.72 ± 1.66	15.80 ± 2.76	30.80 ± 8.49	17.50 ± 5.98	*a, b, c, d, f*
	D_2 [10^{-3} mm^2/s]	2.04 ± 0.08	1.93 ± 0.08	2.15 ± 0.21	1.98 ± 0.11	*b, d, f*
3-comp	$f_{interm.}$ [%]	25.60 ± 4.34	22.40 ± 5.75	30.40 ± 7.67	24.80 ± 8.33	*d, f*
	$f_{fast,3}$ [%]	6.15 ± 2.03	13.20 ± 4.00	26.90 ± 8.83	14.30 ± 6.31	*a, b, c, d, f*
	D_3 [10^{-3} mm^2/s]	1.51 ± 0.10	1.45 ± 0.10	1.12 ± 0.26	1.36 ± 0.21	*b, d, f*

$P < 0.05$ for: *a* cortex vs. medulla; *b* cortex and rest; *c* cortex and tracts; *d* medulla and rest; *e* medulla and tracts; *f* rest and tracts.

ROI-based analysis shows that the fast signal component for biexponential as well as triexponential fitting is most useful to distinguish between different tissue types in the kidneys, which might be due to differences in vascularization between cortex and medulla. Our study did not show significant differences between FA or MD in ROI_{cortex} and $ROI_{medulla}$, as most publications did.[3–10] A reason for this could be the ROI selection method: where most studies use manually drawn ROIs to specifically select ROIs that only contain medullar tissue, we have developed an automated method to eliminate user selection biases. The $ROI_{medulla}$ obtained by this method also includes other regions, most importantly renal columns that do not have the anisotropic tissue structure characteristic of the medulla. This is reflected in the diffusion values we found for the medulla that are higher than typically reported in the literature.

The tractography-based parameters of all models are most similar to those of the medulla, which is in agreement with the widely accepted belief that diffusion anisotropy originates in the radially oriented structures in the medulla.[4–10,12–14,27] However, tract-based FA is significantly higher than ROI-based FA in the medulla. This is a bias of the methods used, where tractography seeks out the highest anisotropy in the area and terminates when FA is too low,

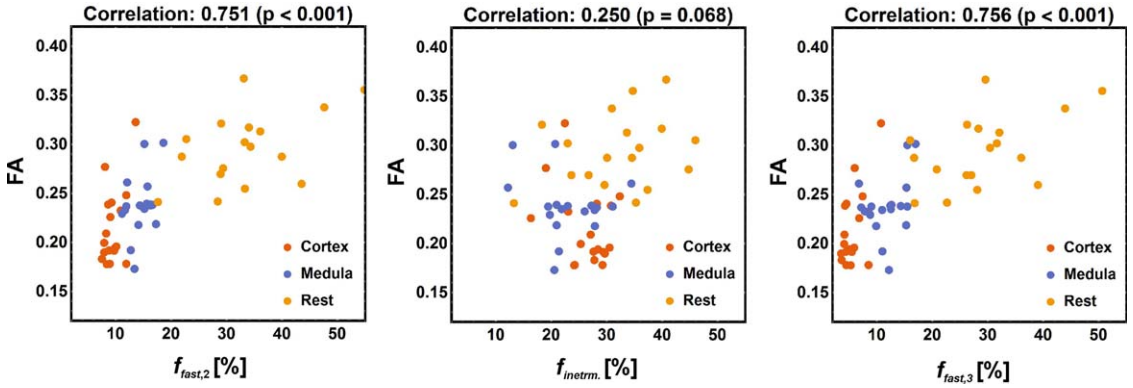

FIGURE 7: Correlation between f_{fast2}, f_{interm}, and f_{fast3} and FA for each of the three ROIs. The correlation values and *P*-values were obtained from Spearman's rank test. Only the f_{fast2} and f_{fast3} showed a high and significant correlation with FA.

pushing FA in the tracts up, whereas our $ROI_{medulla}$ selects the entire inner structure of the kidney, including renal columns, as well as renal pyramids. Furthermore, the tracts were mostly concentrated in the medulla and absent in the renal columns, but this did not result in significant differences between the tracts and cortex either.

We have shown that FA from DTI is correlated to the fast components in bi- and triexponential fits: the higher the signal fraction of the fast component, the higher the FA. This suggests that diffusion anisotropy in the kidneys not only originates in the radially oriented tissue structure of tubules in the kidney medulla, as is usually assumed in kidney diffusion studies, but also in fast water movements, such as perfusion or tubular flow. This is in agreement with an earlier combined DTI and IVIM study concluding that both flow and tissue structure contribute to medullary diffusion anisotropy.[28]

Although we found similar patterns in all our subjects, a limitation of our study is the limited number of subjects and the lack of any clinical information that we could relate to the imaging results. Furthermore, subjects were not given any restrictions on water or food intake, which might have increased the variability of the parameters between subjects. Another limitation to our study is that there is no standard of reference to compare the DTI, mono-, bi-, and triexponential fits with. Therefore, it is impossible to draw any definitive conclusions about which of the mono-, bi-, or triexponential fits best fits the diffusion signal of the kidney, and which model most accurately reflects kidney physiology. It could well be that the different regions of the kidney are best described by different models. The automated method we used for ROI selecting had several advantages, most importantly in eliminating user selection bias and including the whole kidney in ROI analysis. A downside of this method is that the $ROI_{medulla}$ not only included medullar tissue, but renal columnar tissue as well, resulting in an FA that is lower than expected. Our study suggests that anisotropy in both the diffusion and the pseudodiffusion signal components contribute to diffusion anisotropy in the kidneys. To prove this would require fitting a dual or triple tensor model for the bi- and triexponential fit. However, this means fitting for 14 (in a two-tensor model) or 21 (in a three-tensor model) degrees of freedom, for which much more *b*-values and gradient directions with very high data quality are necessary.

In conclusion, triexponential fitting of the signal decay is feasible for the diffusion signal in the kidney, and provides additional information on structures associated with intermediate water flow processes to the IVIM model.

Acknowledgments

Contract grant sponsor: Netherlands Organisation for Scientific Research (NWO); contract grant number: VIDI grant 639.072.411 (to A.L.)

We thank Niels Blancken for technical support and help with data acquisition and Bart Vroling for work on image processing.

References

1. Notohamiprodjo M, Reiser MF, Sourbron SP. Diffusion and perfusion of the kidney. Eur J Radiol 2010;76:337–347.
2. Basser PJ, Pierpaoli C. Microstructural and physiological features of tissues elucidated by quantitative-diffusion-tensor MRI. 1996. J Magn Reson 2011;213:560–570.
3. Heusch P, Wittsack HJ, Pentang G, et al. Biexponential analysis of diffusion-weighted imaging: comparison of three different calculation methods in transplanted kidneys. Acta Radiol 2013;54:1210–1217.
4. Gaudiano C, Clementi V, Busato F, et al. Diffusion tensor imaging and tractography of the kidneys: assessment of chronic parenchymal diseases. Eur Radiol 2013;23:1678–1685.
5. Gurses B, Kilickesmez O, Tasdelen N, Firat Z, Gurmen N. Diffusion tensor imaging of the kidney at 3 Tesla MRI: normative values and repeatability of measurements in healthy volunteers. Diagn Intervent Radiol 2011;17:317–322.
6. Notohamiprodjo M, Glaser C, Herrmann KA, et al. Diffusion tensor imaging of the kidney with parallel imaging: initial clinical experience. Invest Radiol 2008;43:677–685.
7. Wu M, Lin Y, Shieh C, et al. Measuring anisotropic diffusion in kidney using MRI. Acad Radiol 2011;18:1168–1174.
8. Chan RW, von Deuster C, Stoeck CT, et al. High-resolution diffusion tensor imaging of the human kidneys using a free-breathing, multi-slice, targeted field of view approach. NMR Biomed 2014;27:1300–1312.
9. Chuck NC, Steidle G, Blume I, Fischer MA, Nanz D, Boss A. Diffusion tensor imaging of the kidneys: influence of b-value and number of encoding directions on image quality and diffusion tensor parameters. J Clin Imaging Sci 2013;3:1–9.
10. Seif M, Lu H, Boesch C, Reyes M, Vermathen P. Image registration for triggered and non-triggered DTI of the human kidney: Reduced variability of diffusion parameter estimation. J Magn Reson Imaging. 2015;41:1228–1235.
11. Jaimes C, Darge K, Khrichenko D, Carson RH, Berman JI. Diffusion tensor imaging and tractography of the kidney in children: feasibility and preliminary experience. Pediatr Radiol 2014;44:30–41.
12. Lanzman RS, Ljimani A, Pentang G, et al. Kidney transplant: functional assessment with diffusion-tensor MR imaging at 3T. Radiology 2012;266:218–225.
13. Hueper K, Khalifa AA, Bräsen JH, et al. Diffusion-Weighted imaging and diffusion tensor imaging detect delayed graft function and correlate with allograft fibrosis in patients early after kidney transplantation. J Magn Reson Imaging 2016;44:112–121.
14. Lu L, Sedor JR, Gulani V, et al. Use of diffusion tensor MRI to identify early changes in diabetic nephropathy. Am J Nephrol 2011;34:476–482.
15. Le Bihan D, Breton E, Lallemand D, Aubin M-L, Vignaud J, Laval-Jeantet M. Separation of diffusion and perfusion in intravoxel incoherent moting MR imaging. Radiology 1988;168:497–505.
16. Wittsack HJ, Lanzman RS, Mathys C, Janssen H, Modder U, Blondin D. Statistical evaluation of diffusion-weighted imaging of the human kidney. Magn Reson Med 2010;64:616–622.
17. Eisenberger U, Binser T, Thoeny HC, Boesch C, Frey FJ, Vermathen P. Living renal allograft transplantation: diffusion-weighted MR imaging in longitudinal follow-up of the donated and the remaining kidney. Radiology 2013;270:800–808.
18. Gaing B, Sigmund EE, Huang WC, et al. Subtype differentiation of renal tumors using voxel-based histogram analysis of intravoxel incoherent motion parameters. Invest Radiol 2015;50:144–152.
19. Chandarana H, Kang SK, Wong S, et al. Diffusion-weighted intravoxel incoherent motion imaging of renal tumors with histopathologic correlation. Invest Radiol 2012;47:688–696.

20. Ebrahimi B, Rihal N, Woollard JR, Krier JD, Eirin A, Lerman LO. Assessment of renal artery stenosis using intravoxel incoherent motion diffusion-weighted magnetic resonance imaging analysis. Invest Radiol 2014;49:640–646.
21. Ichikawa S, Motosugi U, Ichikawa T, Sano K, Morisaka H, Araki T. Intravoxel incoherent motion imaging of the kidney: alterations in diffusion and perfusion in patients with renal dysfunction. Magn Reson Imaging 2013;31:414–417.
22. Lee CH, Yoo KH, Je BK, et al. Using intravoxel incoherent motion MR imaging to evaluate cortical defects in the first episode of upper urinary tract infections: preliminary results. J Magn Reson Imaging 2014;40:545–551.
23. Kim JW, Lee CH, Yoo KH, et al. Intravoxel incoherent motion magnetic resonance imaging to predict vesicoureteral reflux in children with urinary tract infection. Eur Radiol 2016;26:1670–1677.
24. Wurnig MC, Donati OF, Ulbrich E, et al. Systematic analysis of the intravoxel incoherent motion threshold separating perfusion and diffusion effects: Proposal of a standardized algorithm. Magn Reson Med 2015;74:1414–1422.
25. Barbieri S, Donati OF, Froehlich JM, Thoeny HC. Impact of the calculation algorithm on biexponential fitting of diffusion-weighted MRI in upper abdominal organs. Magn Reson Med 2016;75:2175–2184.
26. Wittsack H-J, Lanzman RS, Quentin M, et al. Temporally resolved electrocardiogram-triggered diffusion-weighted imaging of the human kidney: correlation between intravoxel incoherent motion parameters and renal blood flow at different time points of the cardiac cycle. Invest Radiol 2012;47:226–230.
27. Sigmund EE, Vivier P-H, Sui D, et al. Intravoxel incoherent motion and diffusion-tensor imaging in renal tissue under hydration and furosemide flow challenges. Radiology 2012;263:758–769.
28. Notohamiprodjo M, Chandarana H, Mikheev A, et al. Combined intravoxel incoherent motion and diffusion tensor imaging of renal diffusion and flow anisotropy. Magn Reson Med 2015;73:1526–1532.
29. Van Baalen S, Leemans A, Dik P, ten Haken B, Froeling M. Characterizing the microstructural and architectural organization of healthy kidney tissue using diffusion tensor imaging, fiber tractography and intra-voxel incoherent motion. In: Proc 22nd Annual Meeting ISMRM, Milan; 2014; 22.
30. Cercueil J-P, Petit J-M, Nougaret S, et al. Intravoxel incoherent motion diffusion-weighted imaging in the liver: comparison of mono-, bi-, and tri-exponential modelling at 3.0-T. Eur J Radiol 2015;25:1541–1550.
31. Hayashi T, Miyati T, Takahashi J, et al. Diffusion analysis with triexponential function in liver cirrhosis. J Magn Reson Imaging 2013;38:148–153.
32. Ueda Y, Takahashi S, Ohno N, et al. Triexponential function analysis of diffusion-weighted MRI for diagnosing prostate cancer. J Magn Reson imaging 2016;43:138–148.
33. Seif M, Mani LY, Lu H, et al. Diffusion tensor imaging of the human kidney: Does image registration permit scanning without respiratory triggering? J Magn Reson Imaging 2016;44:327–334.
34. Froeling M, Nederveen AJ, Heijtel DFR, et al. Diffusion-tensor MRI reveals the complex muscle architecture of the human forearm. J Magn Reson Imaging 2012;36:237–248.
35. Leemans A, Jeurissen B, Sijbers J, Jones DK (eds.). ExploreDTI: a graphical toolbox for processing, analyzing and visualizing diffusion MRI data. In: Proc 17th Annual Meeting ISMRM, Honolulu; 2009.
36. Klein S, Staring MM K, Viergever MA, Pluim JPW. Elastix: a toolbox for intensity-based medical image registration. IEEE Trans Med Imaging 2010;29:196–205.
37. Shamonin DP, Bron EE, Lelieveldt BPF, Smits M, Klein S, Staring M. Fast parallel image registration on CPU and GPU for diagnostic classification of Alzheimer's disease. Front Neuroinform 2014;7:1–15.
38. Leemans A, Jones DK. The B-matrix must be rotated when correcting for subject motion in DTI data. Magn Reson Med 2009;61:1336–1149.
39. Yushkevich PA, Piven J, Hazlett HC, et al. User-guided 3D active contour segmentation of anatomical structures: Significantly improved efficiency and reliability. NeuroImage 2006;31:1116–1128.
40. Veraart J, Sijbers J, Sunaert S, Leemans A, Jeurissen B. Weighted linear least squares estimation of diffusion MRI parameters: strengths, limitations, and pitfalls. NeuroImage 2013;81:335–346.
41. Tax CM, Otte WM, Viergever MA, Dijkhuizen RM, Leemans A. REKINDLE: robust extraction of kurtosis INDices with linear estimation. Magn Reson Med 2015;73:794–808.
42. Calamante F, Tournier JD, Heidemann RM, Anwander A, Jackson GD, Connelly A. Track density imaging (TDI): validation of super resolution property. NeuroImage 2011;56:1259–1266.
43. Seif M, Lu H, Boesch C, Reyes M, Vermathen P. Image registration for triggered and non-triggered DTI of the human kidney: Reduced variability of diffusion parameter estimation. J Magn Reson Imaging 2015;41:1228–1235.
44. Froeling M, Oudeman J, Strijkers GJ, et al. Muscle changes detected with diffusion-tensor imaging after long-distance running. Radiology 2014;274:548–562.
45. Stoeck CT, von Deuster C, Genet M, Atkinson D, Kozerke S. Second order motion compensated spin-echo diffusion tensor imaging of the human heart. J Cardiovasc Magn Reson 2015;17:1–3.
46. Vos SB, Jones DK, Jeurissen B, Viergever MA, Leemans A. The influence of complex white matter architecture on the mean diffusivity in diffusion tensor MRI of the human brain. NeuroImage 2012;59:2208–2216.